IEEE Photonics Journal
An IEEE Photonics Society Publication

Open Access

Numerical Model of Chirped Pulse Amplification in Pulsed Synchronously Pumped Low-Repetition-Rate Fiber Amplifiers

Volume 13, Number 3, June 2021

Haitao Zhang
Decai Deng
Jiaqi Zu
Junyu Chen
Dan Li

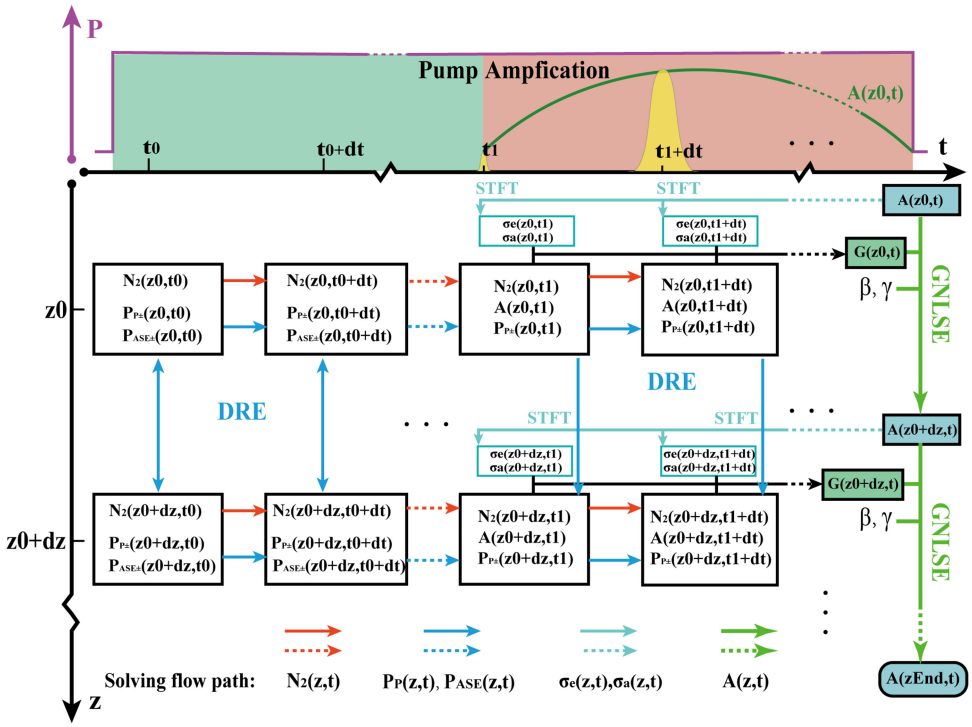

DOI: 10.1109/JPHOT.2021.3075522

Numerical Model of Chirped Pulse Amplification in Pulsed Synchronously Pumped Low-Repetition-Rate Fiber Amplifiers

Haitao Zhang, Decai Deng, Jiaqi Zu, Junyu Chen, and Dan Li

Center for Photonics and Electronics, Department of Precision Instrument,Tsinghua University, Beijing 100084, China

DOI:10.1109/JPHOT.2021.3075522

Manuscript received April 18, 2021; accepted April 22, 2021. Date of publication April 26, 2021; date of current version May 14, 2021. This work was supported by the National Natural Science Foundation of China (NSFC) under Grant 61475081. Corresponding author: Haitao Zhang (e-mail: zhanghaitao@mail.tsinghua.edu.cn).

Abstract: We propose a numerical model to simulate amplification in a pulsed synchronously pumped chirped pulse amplifier (CPA) operating at a low repetition rate. The generalized nonlinear Schrödinger equation and dynamic rate equations are employed to facilitate an accurate treatment of time-space-dependent-gain, wavelength-dependent saturation energy, nonlinearity, and dispersion. Because of an accurate instantaneous gain term, the model can adequately explain pulse distortion and spectral redshift during amplification. The bidirectional amplified spontaneous emission, final output energy, and evolution of temporal and spectral intensities are also investigated through simulations. In addition, a pulsed synchronously pumped CPA fiber system is estbalished to validate the model. The experimental results for the wave shape, spectrum and energy show excellent agreement with those of simulations.

Index Terms: Chirped-pulse amplification, pulsed synchronously pumped, generalized nonlinear Schrödinger equation.

1. Introduction

IN RECENT years, ultrafast fiber lasers have attracted considerable attention in fields of scientific research [1], biomedicine [2], and industry [3], as fibers yield large surface-to-volume ratio, and are compact and alignment-free. The Yb-doped fiber (YDF) laser is a more suitable option among these, owing to its high single-pass gain and low quantum defects [4]. The length of the gain medium in fiber lasers is usually hundreds of times greater than that in solid state lasers; therefore, the gain fiber plays an important role in shaping the temporal and spectral intensities and enhancing the energy [5], [6]. Thus, rigorous study of pulse evolution in gain fibers is necessary for optimizing the performance of an amplifier.

A common approach to simulate pulse propagation in a gain fiber is by adopting the generalized nonlinear Schrödinger equation (GNLSE) with a constant or a scaled gain coefficient according to the pulse energy [7]–[10]. It has been widely used to explain self-similar amplification[8]and the mode-locking process [10]. However, this approach neglects the wavelength-dependent gain, resulting in a deficiency in modeling the gain dispersion in the broadband chirped pulse

amplification. Thus, the gain term is usually modified to a Gaussian or parabolic function of the spectrum [15]–[17], and employed to analyze dissipative soliton resonance [14], or dissipative soliton formation [13], [15], combined with simulated Raman scattering [16]. However, there are two drawbacks of these models: (1) the uniform gain along with the fiber deviates from the practical situation due to inversion level variations and (2) the simple Gaussian or parabolic gain function of spectrum is not an accurate description of the complex processes in the gain fiber. To obtain the space-wavelength-dependent gain coefficient, Huang et al. proposed a combined model that sequentially solves rate equations (REs) and the Ginzburg–Landau equation (GLE) while updating the inversion at each position to determine the gain along the fiber for the GLE [17]. Furthermore, Lindberg presented a model that jointly solves the REs and GNLSE [18]. It directly brings the interplay between the dispersive, nonlinear and pump-relevant effects into the model, making the gain function of the spectrum more accurate. A similar model neglecting the amplified spontaneous emission (ASE) was used by Chen et al. [19]. However, the duration of an ultrashort pulse is always much shorter than the response time of the gain medium; thus, the instantaneous gain used in these models may not be precise. The model proposed by Shen et al. uses a separate gain operator to simulate the space-time-frequency-dependent gain, but the ASE is neglected [20]. These models are aimed at simulating the amplification in high-repetition-rate fiber lasers, in which the population inversion is assumed to reach a steady state, because the interval between the signal pulses is much shorter than the upper level lifetime (denoted by τ) of the excited ions. Therefore, the time derivatives of the upper-level population are neglected in these models. This simplification is no longer applicable in the case of low-repetition-rate amplifiers, particularly those with a repetition rate below $1/\tau$ Hz. In such cases, the pulsed synchronous pumping technology is used to achieve higher pump efficiency and weaken the ASE [6], [25]–[27]. In a pulsed synchronously pumped chirped pulse amplifier(CPA), the gain gap between the leading and trailing edges of the pulse is large, producing a more obvious pulse distortion and spectral frequency shift. The aforementioned models are inadequate for explaining these phenomena induced by the instantaneous gain asymmetry in the time domain. Moreover, the saturation energy usually assumes a constant value and dose not reflect the wavelength dependence of the chirped pulse, leading to an incorrect estimation of the gain saturation of the spectral wings of the pulse, particularly in a broadband CPA.

In this study, we propose a numerical model to simulate the evolution of a chirped pulse in a pulsed synchronously pumped fiber amplifier. The space-time-dependent gain coefficient is calculated by using dynamic rate equations (DREs) combined with the wavelength-dependent saturation energy derived by short-time Fourier transform (STFT) method. Moreover, the ASE power distribution is calculated by this model according to boundary conditions, to optimize the fiber amplifier operating at a low repetition rate. The GNLSE, modified with the space-time-dependent gain is employed to simulate the pulse and spectrum evolutions during amplification. Our model integrates instantaneous gain, ASE, and wavelength-dependent gain saturation to precisely determine chirped pulse propagation. In addition, a synchronously pumped CPA system is established to validate the model. The pulse evolution process in the CPA system is successfully simulated and shows good agreement with the experimental results.

2. Theory

2.1. Dynamic Rate Equation

To simulate a low-repetition-rate fiber amplifier, the transient pumping process and ASE should be considered. Here, we adopted the DRE with multiple wavelength channels. In the YDF amplifier, the DRE can be expressed as [18]

$$\frac{\partial N_2(z,t)}{\partial t} = \frac{1}{hcA_c}\Gamma_p\lambda_p\left[\sigma_a\left(\lambda_p\right)N_1(z,t) - \sigma_e\left(\lambda_p\right)N_2(z,t)\right]P_p^{\pm}(z,t) - \frac{N_2(z,t)}{\tau}$$
$$+ \frac{1}{hcA_c}\Gamma_s\lambda_s\left[\sigma_a\left(\lambda_s\right)N_1(z,t) - \sigma_e\left(\lambda_s\right)N_2(z,t)\right]P_s^{\pm}(z,t)$$

$$+\frac{1}{hcA_c}\sum_{k=1}^{K}\Gamma_k\lambda_k\left[\sigma_a(\lambda_k)N_1(z,t)-\sigma_e(\lambda_k)N_2(z,t)\right]P_k^{\pm}(z,t), \tag{1}$$

$$\frac{\partial P_{k,s}^{\pm}(z,t)}{\partial z}\pm\frac{1}{v_g(\lambda_{k,s})}\frac{\partial P_{k,s}^{\pm}(z,t)}{\partial t}=\pm\Big(\Gamma_{k,s}\left[\sigma_e(\lambda_{k,s})N_2(z,t)-\sigma_a(\lambda_{k,s})N_1(z,t)\right]P_{k,s}^{\pm}(z,t)$$
$$-\alpha_{k,s}P_{k,s}^{\pm}(z,t)+\Gamma_k\sigma_e(\lambda_k)N_2(z,t)2hc^2\Delta\lambda/\lambda_k^3\Big) \tag{2}$$

$$\frac{\partial P_p^{\pm}(z,t)}{\partial z}\pm\frac{1}{v_g(\lambda_p)}\frac{\partial P_p^{\pm}(z,t)}{\partial t}=\Gamma_p\left(\sigma_a(\lambda_p)N_2(z,t)-\sigma_e(\lambda_p)N_1(z,t)\right)P_p^{\pm}(z,t)-\alpha_pP_p^{\pm}(z,t) \tag{3}$$

$$N_T=N_1(z,t)+N_2(z,t), \tag{4}$$

where N_T, $N_1(z,t)$, $N_2(z,t)$are the total dopant number density and space-time-dependent lower and upper energy populations, respectively. h is the Planck's constant, c is the speed of light in vacuum, τ is the upper-state lifetime, z denotes the position along the fiber, t denotes the temporal coordinate, α is the background loss in the fiber, and P is the power. Subscripts "+" and "-" correspond to forward and backward propagating directions, the subscripts "p", "s", and "k" correspond to pump, signal, and ASE pulse. Γ represents the geometric overlap factor and Γ_P is approximated by the ratio of the core and cladding areas for double cladding fibers. A_c is the area of the doping region, which is usually equal to the cross-sectional area of the fiber core, v_g donates the group velocity. The walk off between pump and signal light can be neglected in short length gain fibers. σ_a and $\sigma_e$represent wavelength-dependent effective absorption and emission cross sections, respectively, and are provided by the fiber manufacturer. The last term on the right-hand side of Eq. (1) and the third term in Eq. (2) represent the spontaneous emission, where $\Delta\lambda$ is wavelength resolution. The evolutions of signal and ASE are described by the Eq. (2). The only difference is that an initial value of zero is assumed for ASE, whereas an injected power $P_s(t)|_{z=0}$ is assigned as the initial value for the signal. In addition, the initial value of pump light $P_p(t)|_{z=0}$, i.e., the pump power at both ends, is known as the initial condition of the DRE. The ASE power signifies the total power over the entire ASE spectrum after the signal pulse has passed through the fiber. We considered only the fundamental mode and utilized the finite difference method to solve the partial differential equation.

2.2. Generalized Nonlinear Schrödinger equation

The DRE was only used to simulate the intensity profile rather than the complex amplitude. To describe the evolution of the complex electric field envelope of the light, the GNLSE is usually applied. A form of the GNLSE including dispersion, self-phase modulation, gain effect, self-steepening, and simulated Raman scattering is given as follows [11]:

$$\frac{\partial A}{\partial z}=\frac{G(z,T)-\alpha}{2}A-\frac{i\beta_2}{2}\frac{\partial^2A}{\partial T^2}+\frac{\beta_3}{6}\frac{\partial^3A}{\partial T^3}+i\gamma(\omega_0)$$
$$\times\left(1+\frac{i}{\omega_0}\frac{\partial}{\partial T}\right)A\int_{-\infty}^{\infty}R(\tau)|A(z,T-\tau)|^2d\tau \tag{5}$$

where A is the complex field envelope of the pulse, and z and T are the positions along the fiber and retarded time, respectively. $G(z,t)$ is the space-time-dependent gain that was calculated by using the DRE, and the details are introduced in section 2.3. β_2 and β_3 are the group velocity dispersion and third-order dispersion, respectively. $\gamma(\omega_0)=\omega_0n_2/(cA_{eff})$ denotes the nonlinear parameter, where A_{eff} is the effective mode area, n_2 is the Kerr refractive index coefficient, and ω_0 is the center frequency of the laser. The nonlinear response function is given by $R(T)=(1-f_R)\delta(T)+f_Rh_R(T)$, where $h_R(T)=(T_1^2+T_2^2)/(T_1T_2^2)\exp(-T/T_2)\sin(T/T_1)$. To simulate silica fibers, $T_1=12.2fs$, $T_2=32fs$ and $f_R=0.18$ are derived from Raman gain spectrum, based on a previous study [25]. $\alpha$is the intrinsic loss of the fiber.

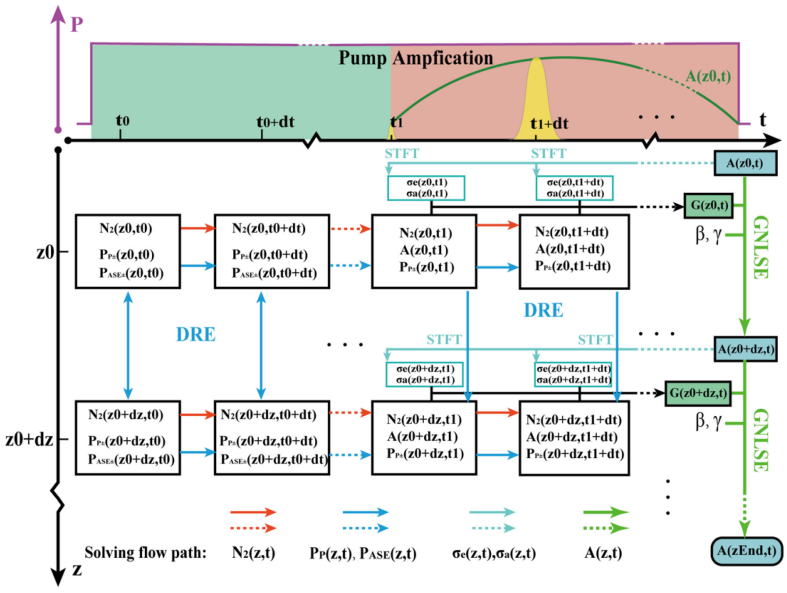

Fig. 1. Schematic illustration of the numerical model. STFT: Short-time Fourier transform, GNLSE: generalized nonlinear Schrödinger equation.

2.3. Our Numerical Model

In a low-repetition-rate YDF laser, the synchronous pumping technology is usually adopted to suppress the ASE. The time elapsing between consecutive pump-pulses is usually greater than the lifetime of the upper level. This implies that the upper-level propagation, $N_2(z)$, will evolve between consecutive pulses and not reach a steady-state profile [18], [19]. Therefore, our numerical model was divided into two main processes: (1) pump and (2) amplification, as shown in Fig. 1.

The relative position between the pump and signal pulses influences the ASE power. When the pump pulse is fixed, the signal pulse is closer to the leading edge of the pump pulse, and less ASE power is generated; however, the magnification of the signal is smaller, as the pump pulse behind the signal pulse is of no use. The signal pulse is generally located at the tail of the pump pulse in pulsed synchronously pumped amplifiers to obtain greater population inversion, and we adopted this arrangement in our model. The pumping process started at t_0 and ended at t_1. During this time, the DRE was solved by using the finite difference method without any signal input. Finally, the initial conditions, i.e., the state at t_1 required for amplification, were assessed, such as the upper-level population, $N_2(z, t_1)$, at each position of the fiber pump power distribution, $P_p^{\pm}(z, t_1)$, and ASE power distribution, $P_{ASE}^{\pm}(z, t_1)$. The amplification process began at t_1, and during this stage, the pump continued to operate until the end of the seed signal; we combined the DRE and GNLSE with a chirped-pulse as the input signal. It must be noted that the phase of the input pulse should be known or reconstructed by combining the pulse intensity envelope and spectrum. Moreover, the wavelength of the chirped pulse, denoted by $\lambda(t)$, varies with time; thus, the absorption and emission cross sections in Eq. (1) at different times cannot be described as the same σ_a and σ_e, respectively. Therefore, we modified Eq. (1) as follows:

$$\frac{\partial N_2(z,t)}{\partial t} = \frac{1}{hcA_c}\Gamma_p\lambda_p\left[\sigma_a\left(\lambda_p\right)N_1(z,t) - \sigma_e\left(\lambda_p\right)N_2(z,t)\right]P_p^{\pm}(z,t) - \frac{N_2(z,t)}{\tau} + \frac{1}{hcA_c}\Gamma_s\lambda_s\left[\sigma_a\left(\lambda(t)\right)N_1(z,t) - \sigma_e\left(\lambda(t)\right)N_2(z,t)\right]P_s^{\pm}(z,t) \quad (6)$$

Because the amplification stage is only of the order of nanoseconds, which is much shorter than the duration of the pump stage, the accumulation of the ASE during the amplification stage is

negligible, and the final ASE result is represented by the ASE output of the pumping process. In our model, the instantaneous wavelength, $\lambda(t)$, was obtained by using STFT method, according to the chirped-pulse signal with phase information. We used many "soft" window functions, as depicted in the yellow area at the top of Fig.1, to cut the temporal pulse trace in the time domain [26]. We applied the FFT to each temporal splice, in succession, to obtain the center wavelength. The window was small enough to ensure the accuracy of $\lambda(t)$. Combining Eqs. (2–4) and (6) and the initial conditions calculated in the pumping process, we updated the value of $N_2(z_0, t)$ and used it to determine the space-time-dependent small signal gain coefficient, expressed as follows:

$$g(z, \mathrm{t}) = \Gamma_s \left[\left(\sigma_e(\lambda(t)) + \sigma_a(\lambda(t)) \right) N_2(z, t) - \sigma_a(\lambda(t)) N_T \right] - \alpha_s. \tag{7}$$

The gain saturation effect can also influence the evolution of the pulse and must be included in the GNLSE. In contrast to previous studies [16], [18], in which, the gain saturation was only treated in the time domain, i.e., the used saturation energy was a constant value, the time- and wavelength-dependent gain were considered simultaneously in this study; therefore, the gain function was modified as:

$$G(z, t) = g(z, t) \exp\left(-\frac{A_{eff}}{E_{sat}} \int_{-\infty}^{T} |A(z, \tau)|^2 d\tau \right), \tag{8}$$

where the wavelength-dependent saturation energy, E_{sat}, is expressed as $E_{\mathrm{sat}} = A_{\mathrm{eff}} hc/\Gamma_k \lambda(t)(\sigma_e(\lambda(t)) + \sigma_a(\lambda(t)))$. Thus, the space-time-dependent gain with substantial gain saturation in amplifiers was described adequately. This method is applicable only when the spectral components are well-separated in time but not work in the case of Raman scattering, for example. Using these parameters, we calculated the GNLSE to propagate the pulse and used Eqs. (2) and (3) to propagate the pump power.

Generally, the GNLSE is solved by applying the standard fourth-order Runge-Kutta in the interaction picture(RK4IP) method [27], or split-step Fourier method [11]. For computational accuracy, the RK4IP method was applied in this paper. In this paper, dispersive effects and nonlinear effects are evaluated separately in the time domain and Fourier domain. Thus, the GNLSE can be represented in the following form:

$$\frac{\partial A}{\partial z} = (\hat{D} + \hat{N})A, \tag{9}$$

where $\hat{D}$ and $\hat{N}$ represent the dispersive operators and nonlinear operators, respectively. They are expressed by

$$\begin{aligned} \hat{D} &= \frac{i\beta_2 \partial^2}{2\partial T^2} - \frac{\beta_3 \partial^3}{6\partial T^3}, \\ \hat{N} &= \frac{G(z, T) - \alpha}{2} + i\gamma\,(\omega_0)\,\frac{1}{A}\left(1 + \frac{i}{\omega_0}\frac{\partial}{\partial T}\right) A \int_{-\infty}^{\infty} R(\tau)|A(z, T-\tau)|^2 d\tau. \end{aligned} \tag{10}$$

Finally, the solved complex field envelope, $A(z_0 + dz, t)$, was used to update the instantaneous power of the pulse: $P_s(z_0 + dz, t)$, in Eq. (6) by $P_s(z_0 + dz, t) = |A(z_0 + dz, t)|^2$. Thus, the final output pulse was obtained by alternately solving the DRE and GNLSE. In addition, to ensure consistency of the time frame, the gain function, $G(z, t)$, calculated by using the DRE was converted to $G(z, T)$ according to the relation $T = t - z/v_g$.

3. Experimental Setup

As shown in Fig. 2, we established a CPA fiber system to validate our model. The oscillator was an all-polarization-maintaining all-normal-dispersion fiber laser with a nonlinear loop amplifier mirror as a mode locker, as reported in our previous work [28]. It had a repetition rate of 8.2 MHz, pulse duration of 35 ps and spectral width of 22 nm. The seed pulses were divided into two beams with a splitting ratio of 98:2. The weaker pulse was probed by using a photon detector (PD),

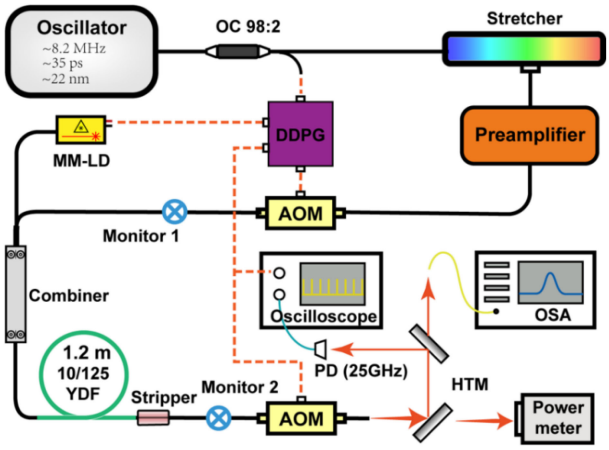

Fig. 2. Schematic of the experimental setup, OC: output coupler, DDPG: digital delay and pulse generator, AOM: acoustic optical modulator, MM-LD: multi-mode laser diode, PD: photodetector, HTM: highly transmitting mirror.

and it served as the temporal reference signal for the digital delay and pulse generator (DDPG). The output signals from the DDPG were used to drive the acoustic optical modulators (AOMs) and laser diode with an accurate adjustment of time delay. The other pulse was injected into the subsequent stretcher composed of an optical circulator and a reflecting chirped fiber Bragg grating that supplied a group delay dispersion of 40 ps^2 and third-order dispersion of -0.5 ps^3, respectively. Highly chirped pulses were produced in this manner. A preamplifier was added after the stretcher to compensate for the loss in the stretcher and AOM. The AOM at the top in Fig. 2 was used as a pulse picker, after which the repetition rate is decreased to 1 kHz. The following amplifier as the protagonist in this experiment is employed with synchronously pump technology. The chirped pulses from the AOM were fed into a segment of a double-clad YDF (PLMA-YDF-10/125-VIII, Nufern) by a combiner, using a 25 W 976 nm multimode laser diode (MM-LD) as the pump. A stripper is connected at the end of the gain fiber to peel the cladding light mainly composed of unabsorbed pump light. Another AOM was used to filter the forward ASE raised in the last amplifier by setting a proper temporal gate. Thus, the output energy of the forward ASE was obtained by subtracting the energy at monitor 2 from the final output. Finally, two highly transmitting mirrors (HTM) were placed to distribute the pulses to different measuring devices, such as a power meter, an optical spectrum analyzer (OSA) and an oscilloscope. In addition, the signal at monitor 1 was detected by these instruments.

4. Results and Discussion

The input pulse information was obtained at monitor 1, and the pulse duration is of approximately 1.35 ns was detected by a high-speed oscilloscope (bandwidth 40GHz, Agilent) together with a fast photodetector (bandwidth 25 GHz, New Focus Mode-1414). This is illustrated by the blue line at the top of Fig. 3. The spectrum with a bandwidth of approximately 20 nm was measured by the OSA at a spectral resolution of 0.5 nm, shown on the right side of Fig. 3. The energy at monitor 1 was 75 nJ; combined with the measured temporal envelope and spectral profile, the actual temporal and spectral intensities were calculated. However, these data are not sufficient for developing the numerical model as the phase of the input pulse is also required to depict the complex electric envelope. To obtain the phase information, frequency-resolved optical gating (FROG) and spectral phase interferometry for direct electric field reconstruction (SPIDER) are the most popular approaches. However, the input pulse had a low average power and peak power at a low repetition rate after the pulse picker, which was below the measured sensitivity

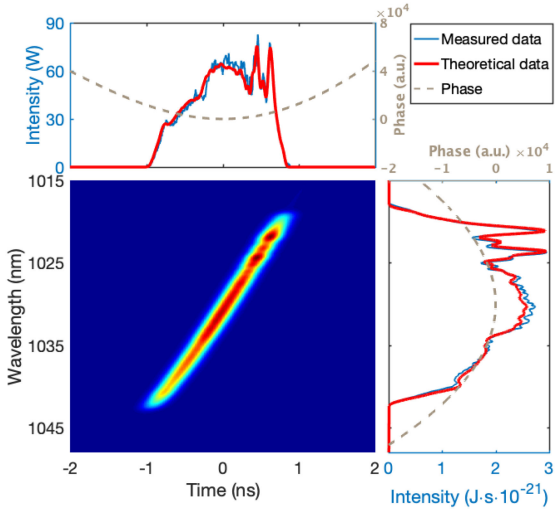

Fig. 3. Theoretical retrieved spectrogram projected onto the temporal intensity and spectrum of the pulse detected at monitor 1. The blue and red lines represent the measured and theoretical data, respectively. The gray dashed lines denote the retrieved phase.

TABLE 1
Parameters Used in the Simulation

Symbol	Value	symbol	value
λ_p	$968nm$	τ	$0.84ms$
λ_s	$1030nm$	n_2	$2.6\times10^{-20}m^2/W$
Γ_p	0.0077	α_p	$5\times10^{-3}m^{-1}$
Γ_s	0.82	α_s	$5\times10^{-3}m^{-1}$
N_T	$8\times10^{25}m^{-3}$	$\Delta\lambda$	$1nm$
σ_a^p	$4.6\times10^{-25}m^2$	β_2	$24.5ps^2/km$
σ_e^p	$3.3\times10^{-25}m^2$	β_3	$0.026ps^3/km$

of these measurements. Therefore, a reconstruction algorithm integrated by the chirp-coefficient iteration and bisection methods was applied [29]. After several iterations, the spectral and temporal phase-intensity functions were successfully retrieved for the chirped pulse plotted by gray dash lines in Fig. 3. The reconstructed temporal and spectral intensities represented by the red lines are in a good agreement with the measured data. In addition, it's obvious from the retrieved spectrogram that the pulses exhibit a linear positive chirp as shown in the bottom left part of Fig. 3.

In the validation experiment, the MM-LD was synchronously driven operating at a wavelength of 968 nm, which was different from the continuous working at 975 nm. The peak power was fixed at 25 W with a pumping duration of 50 μs. The YDF was 1.2 m long with an absorption coefficient of 4.8 dB/m at 975 nm and NA of 0.075, whose core and cladding diameters were 11 μm and 125 μm, respectively. The ion-doping concentration of the YDF related to the absorption coefficient was calculated by using $N_T = \alpha/[10\sigma_a(\lambda_p)\Gamma_p \lg e]$. In this case, clad pumping was applied and $\Gamma_p \approx A_{core}/A_{clad}$. The other parameters used in the simulation are listed in Table 1.

During the pumping process, the energy stored in the YDF and total energy of the ASE were plotted as functions of the pump time, as shown in Fig. 4 (b) . The stored energy increased linearly, whereas the ASE energy increased exponentially; this is why synchronous pumping with a short duration was adopted in this amplifier. At the end of the pumping process, the stored energy was

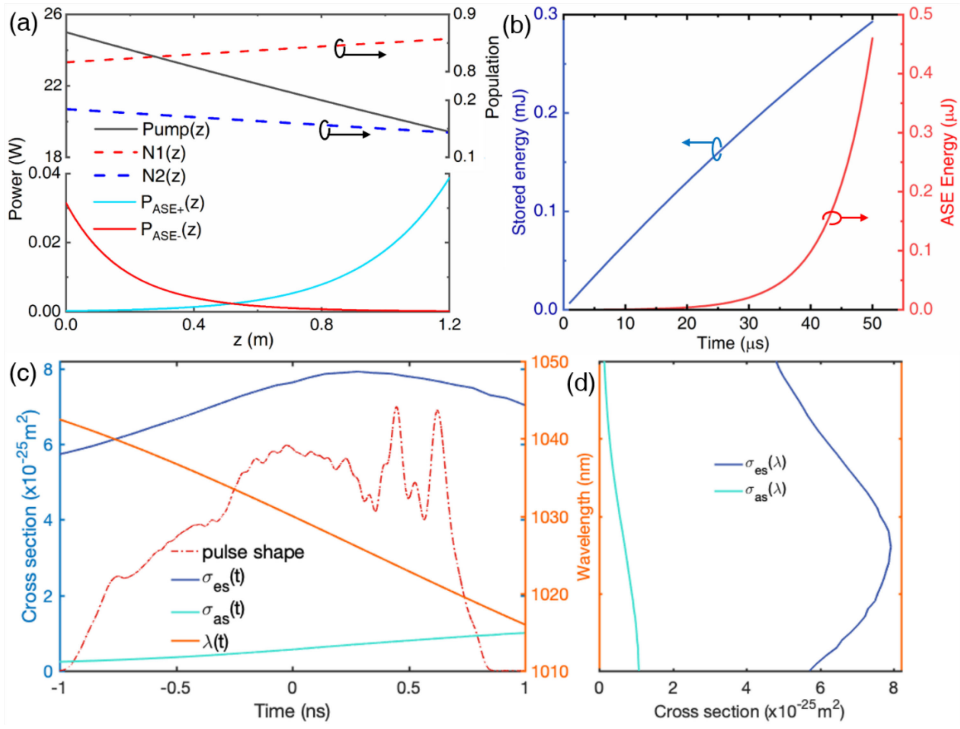

Fig. 4. (a) Distributions of pump power, forward ASE power, backward ASE power upper level population(N_2) and lower level population(N_1) along the fiber after the pumping process, denoted by black, cyan, red, blue dashed and red dashed lines, respectively. (b) Variation in energy stored in the YDF (blue line) and total ASE output energy (red line) with pump time. (c) Instantaneous wavelength (orange line) and instantaneous induced temporal cross sections (blue line denotes emission cross section and cyan line denotes absorption cross section) in the pulse region. (d) Wavelength-dependent cross sections of the YDF provided by Nufern Inc.

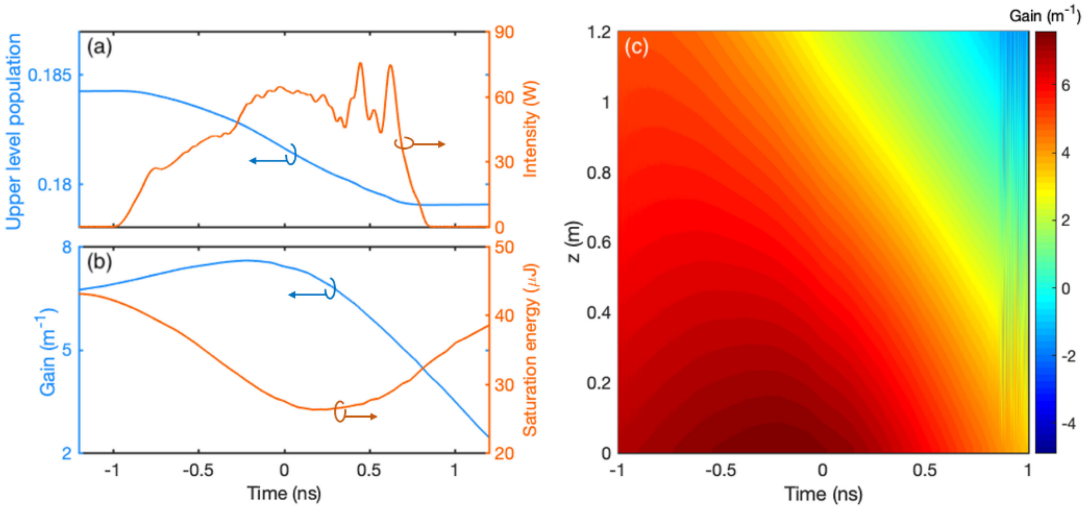

Fig. 5. (a) Temporal upper-level population proportion (blue line) and the temporal intensities of the chirped pulse (orange line). (b) Instantaneous gain (blue line) and instantaneous saturation energy (orange line) in the pulse region at position z = 0. (c) Precise temporal gain, $g(z, t)$, in the YDF during the amplification process.

0.29 mJ, which was nearly 600 times larger than the total ASE energy of 0.45 μJ. With less ASE depleting the reverse population, the pump power exhibited linear absorption shown at the top of Fig.4 (a), and the residual pump was leaked out by the stripper. We can see at the bottom of Fig.4 (a) that the forward ASE and backward ASE have approximately symmetrical distribution curves along the fiber with about an average power of 35 mW at each end of the fiber. Thus, the energy of the forward ASE (0.23 μJ) was approximately half of the total ASE energy, which is close to the experiment value of 0.28 μJ. The distributions of the upper- and lower-level populations ($N_2(z, t_1)$, $N_1(z, t_1)$, t_1, t_1 is the same as in Fig.1 and represents the time when the signal is applied) were also plotted according to the DREs, as shown at the top of Fig.4 (a) by red and blue dashed lines, respectively. The final state data in the pump progress were used as the initial conditions in the amplification process.

In the amplification process, Eq. (5) was used to precisely simulate the temporal and spectral evolutions of the pulse, solved by the RK4IP method. Here, the spatial calculation step size was set to 0.001 m to ensure accuracy. The instantaneous gain coefficient was recalculated at each segment using Eqs. (7) and (8). For example, there were three steps to obtain the instantaneous gain coefficient at the incident end of the YDF, i.e., z $= 0$. First, the instantaneous wavelength $\lambda(t)$ was derived and plotted by applying a STFT method to the complex electronic envelope of the input pulse, as shown by the orange line in Fig.4(c). The instantaneous wavelength decreased nearly in the pulse region from 1042 nm to 1018 nm, which is in agreement with the spectrogram shown in Fig.3. Corresponding to the instantaneous wavelength, the absorption and emission cross sections provided by Nufern were plotted and represented by the cyan and blue solid lines, respectively, in Fig.4 (d). Then, according to the wavelength-dependent cross sections, the instantaneous cross sections ($\sigma_a(\lambda(t))$and $\sigma_e(\lambda(t))$) induced by the instantaneous wavelength were obtained, as shown in Fig.4(c). Second, the temporal cross sections were substituted into Eq. (6). Combined with the initial conditions ($N_2(0, t_1)$, $N_1(0, t_1)$and $P_p(0, t_1)$), the instantaneous $N_2(0, t)$ was obtained as shown in Fig.5(a). Finally, the variation in the small signal gain coefficient with time was determined using Eq. (7), as depicted by the blue line in Fig.5 (b). The maximum instantaneous gain of almost 7.5 m^{-1} was obtained at approximately t $= -200$ ps. The time-dependent saturation energy induced by the instantaneous wavelength was plotted by orange line in Fig.5 (b), which is used to modify the gain coefficient using Eq. (8). Thus, the GNLSE was applied to solve the pulse propagating through the next segment. In a similar manner, the precise instantaneous gain, $g(z, t)$, along the YDF was calculated during the amplification process as depicted in Fig.5(c). The evolution of the gain coefficient at the pulse trailing edge along the path of propagation from the positive-gain to the reabsorption region was evident. The gain profiles in the time domain were essentially convex around the center of the time but decreased as the pulse propagated toward the end of the YDF.

Figs 6 (a) and (b) depict the evolution of the temporal and spectral intensities of the propagating pulse, respectively. It can be seen from the entire evolution that middle region of the pulse is significantly amplified, accompanied by the apparent gain narrowing effect due to the ridge of the gain profile. Moreover, the leading edge of the pulse is evidently amplified by depleting the majority of the reverse population in the pulse region toward the end of the YDF, whereas the trailing edge suffers from laser-reabsorption. Consequently, a red shift of the center wavelength occurs in the spectrum. The final output temporal and spectral intensities are shown in Figs.6(c) and (d), respectively. The results of the simulations of our model were in excellent agreement with the experimental results. The center wavelength was redshifted from 1030 nm to 1033 nm, and the spectrum width is reduced to 13.5 nm due to gain narrowing, as shown in Fig.6 (d). The simulated output pulse energy was calculated by using $E_s = \int_{-\tau_r/2}^{\tau_r/2} |A(L, t)|^2 dt = 1.42\,\mu J$, and this agreed with the measured pulse energy (1.38 μJ) within the acceptable error tolerance. A simulation of the combined GLE and RE was also conducted, where the gain coefficient is calculated by the RE without modification and the saturation energy, E_{sat}, was not wavelength-dependent, expressed as $E_{\text{sat}} = A_{\text{eff}} hc/\Gamma_k \lambda_0(\sigma_e(\lambda_0) + \sigma_a(\lambda_0))$, where λ_0 is the center wavelength. The results are plotted as orange dashed lines in Figs. 6(c) and (d). Although the simulated energy of 1.51 μJ was close to the experimental result with an obvious spectrum narrowing, the waveform differed significantly

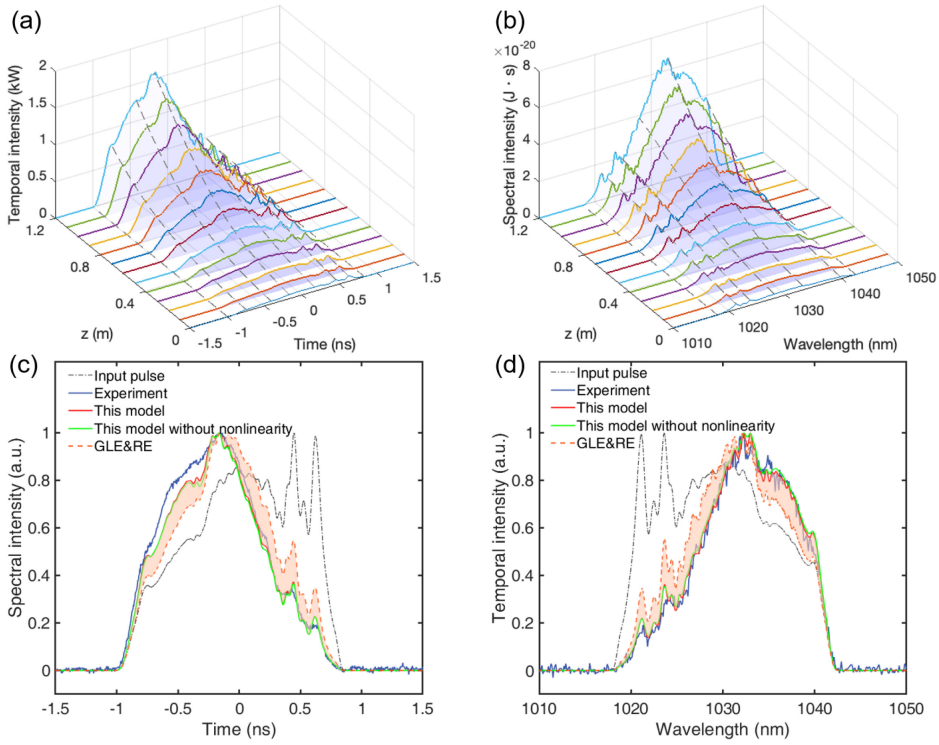

Fig. 6. Evolutions of (a) temporal and (b) spectral intensities of the propagating pulse. (c) Temporal and (d) spectral intensities of the final output, in which the blue, red, green, and orange dashed lines represent the experimental, our model simulation, our model without nonlinearity simulation and the GLE & RE simulation results, respectively.

from the measured shape. Moreover, the red shift of the spectrum was not well manifested by the simulation. The difference between the simulations of our model and the GLE & RE model, denoted by the faint orange areas in Figs.6(c) and (d) indicated the effect induced by the instantaneous gain asymmetry in the time domain and wavelength-dependent saturation energy. The green lines represent the results where our model does not consider the nonlinear effects. It can be seen that the nonlinear effects only cause a weak spectral modulation and are negligible in this experiment.

5. Conclusion

In this study, a numerical model was developed to simulate the propagation of chirped-pulses in a synchronously pumped fiber amplifier. DREs were applied to calculate the distributions of pump power, reverse population, and ASE along the fiber in the pumping process. The results are treated as the initial conditions of the GNLSE in the amplification process. The GNLSE was solved by appling the RK4IP method where the instantaneous gain was updated at each segment according to the DRE and complex filed envelope of the pulse. To validate the model, a synchronously pumped CPA system was established. Chirped pulses having an energy of 75 nJ and a repetition rate of 1 kHz were fed into the gain fiber. The output energy of the forward ASE and signal were 0.28 μJ and 1.38 μJ, which are almost equal to the corresponding simulation results of 0.23 μJ and 1.42 μJ, respectively. Moreover, the output waveform and spectrum were in good agreement with the simulations. Thus, we expect that this model is well-suited for simulating pulse evolutions in the context of a pulsed synchronously pumped CPA system, particularly for low-repetition-rate pulse sequences. Furthermore, it can serve as a valuable tool in optimizing a CPA system, for instance,

by appropriate wave pre-shaping to compensate for the distortion induced by gain narrowing and spectral redshift effects.

References

[1] M. Krebs, *et al.*, "Towards isolated attosecond pulses at megahertz repetition rates," *Nature Photon.*, vol. 7, no. 7, pp. 555–559, 2013.

[2] N. Nishizawa, Y. Chen, P. Hsiung, E. P. Ippen, and J. G. Fujimoto, "Real-time, ultrahigh-resolution, optical coherence tomography with an all-fiber, femtosecond fiber laser continuum at 1.5 μm," *Opt. Lett.*, vol. 29, no. 24, pp. 2846–2848, 2004.

[3] L. Shah, M. E. Fermann, J. W. Dawson, and C. P. J. Barty, "Micromachining with a 50 w, 50 μJ, subpicosecond fiber laser system," *Opt. Exp.*, vol. 14, no. 25, pp. 12546–12551, 2006.

[4] R. Paschotta, J. Nilsson, A. C. Tropper, and D. C. Hanna, "Ytterbium-doped fiber amplifiers," *IEEE J. Quantum Electron.*, vol. 33, no. 7, pp. 1049–1056, Jul. 1997.

[5] D. N. Schimpf, J. Limpert, and A. Tünnermann, "Controlling the influence of SPM in fiber-based chirped-pulse amplification systems by using an actively shaped parabolic spectrum," *Opt. Exp.*, vol. 15, no. 25, pp. 16945–16953, 2007.

[6] D. N. Papadopoulos, M. Hanna, F. Druon, and P. Georges, "Compensation of gain narrowing by self-phase modulation in high-energy ultrafast fiber chirped-pulse amplifiers," *IEEE J. Sel. Topics Quantum Electron.*, vol. 15, no. 1, pp. 182–186, Jan. 2009.

[7] P. K. Mukhopadhyay, K. Ozgoren, I. Levent Budunoglu, and F. O. Ilday, "All-fiber low-noise high-power femtosecond Yb-fiber amplifier system seeded by an all-normal dispersion fiber oscillator," *IEEE J. Sel. Topics Quantum Electron.*, vol. 15, no. 1, pp. 145–152, Jan. 2009.

[8] M. E. Fermann, V. I. Kruglov, B. C. Thomsen, J. M. Dudley, and J. D. Harvey, "Self-similar propagation and amplification of parabolic pulses in optical fibers," *Phys. Rev. Lett.*, vol. 84, no. 26, pp. 6010–6013, 2000.

[9] J. Limpert, *et al.*, "High-power femtosecond Yb-doped fiber amplifier," *Opt. Exp.*, vol. 10, no. 14, pp. 628–638, 2002.

[10] A. Chong, W. H. Renninger, and F. W. Wise, "Properties of normal-dispersion femtosecond fiber lasers," *J. Opt. Soc. Amer. B*, vol. 25, no. 2, pp. 140–148, 2008.

[11] G. P. Agrawal, and H. A. Haus, "Applications of nonlinear fber optics," *Phys. Today*, vol. 55, pp. 58, 2002.

[12] K. Staliunas, "Laser Ginzburg-Landau equation and laser hydrodynamics," *Phys. Rev. A*, vol. 48, no. 2, pp. 1573–1581, 1993.

[13] N. Akhmediev, J. M. Soto-Crespo, M. Grapinet, and Ph. Grelu, "Dissipative soliton interactions inside a fiber laser cavity," *Opt. Fiber Technol.*, vol. 11, no. 3, pp. 209–228, 2005.

[14] D. Li, D. Tang, L. Zhao, and D. Shen, "Mechanism of dissipative-soliton-resonance generation in passively mode-locked all-normal-dispersion fiber lasers," *J. Lightw. Technol.*, vol. 33, no. 18, pp. 3781–3787, 2015.

[15] L. M. Zhao, C. Lu, H. Y. Tam, P. K. A. Wai, and D. Y. Tang, "Gain dispersion for dissipative soliton generation in all-normal-dispersion fiber lasers," *Appl. Opt.*, vol. 48, no. 27, pp. 5131–5137, 2009.

[16] G. P. Agrawal, "Effect of gain dispersion and stimulated raman scattering on soliton amplification in fiber amplifiers," *Opt. Lett.*, vol. 16, no. 4, pp. 226–228, 1991.

[17] Z. Huang, *et al.*, "Combined numerical model of laser rate equation and ginzburg–landau equation for ytterbium-doped fiber amplifier," *J. Opt. Soc. Amer. B*, vol. 29, no. 6, pp. 1418–1423, 2012.

[18] R. Lindberg, P. Zeil, M. Malmström, F. Laurell, and V. Pasiskevicius, "Accurate modeling of high-repetition rate ultrashort pulse amplification in optical fibers," *Sci. Rep.*, vol. 6, no. 1, pp. 34742, 2016.

[19] H. W. Chen, J. Lim, S.-W. Huang, D. N. Schimpf, F. X. Kärtner, and G. Chang, "Optimization of femtosecond Yb-doped fiber amplifiers for high-quality pulse compression," *Opt. Exp.*, vol. 20, no. 27, pp. 28672–28682, 2012.

[20] Y. Shen, G. Gao, Y. Meng, X. Fu, and M. Gong, "Gain-phase modulation in chirped-pulse amplification," *Phys. Rev. A*, vol. 96, no. 4, pp. 043851, 2017.

[21] D. Deng, H. Zhang, Q. Gong, L. He, and J. Zu, "112- μ j 180-fs pulses at 1-kHz repetition rate from Yb-doped laser based on strictly all-fiber CPA structure," *IEEE Photon. J.,* vol. 11, no. 6, Aug. 2019, Art. no. 1505507.

[22] C. Zheng, H. T. Zhang, W. Y. Cheng, M. Liu, P. Yan, and M. L. Gong, "Single mode MOPA structured all-fiber yb pulse fiber amplifier at low repetition," *Laser Phys,* vol. 21, no. 6, pp. 1081, 2011.

[23] M. Y. Cheng, Y. C. Chang, A. Galvanauskas, P. Mamidipudi, R. Changkakoti, and P. Gatchell, "High-energy and high-peak-power nanosecond pulse generation with beam quality control in 200-μm core highly multimode Yb-doped fiber amplifiers," *Opt. Lett.*, vol. 30, no. 4, pp. 358–360, 2005.

[24] M. Liu, B. M. Zhang, P. P. Shum, and X. Cheng, "Pulsed pumping for pulsewidth tunable nanosecond ytterbium-doped fiber laser," *IEEE Photon. Technol. Lett.*, vol. 28, no. 24, pp. 2842–2845, Dec. 2016.

[25] R. H. Stolen, J. P. Gordon, W. J. Tomlinson, and H. A. Haus, "Raman response function of silica-core fibers," *JOSA B*, vol. 6, no. 6, pp. 1159–1166, 1989.

[26] R. Paschotta, "Modeling of ultrashort pulse amplification with gain saturation," *Opt. Exp.*, vol. 25, no. 16, pp. 19112–19116, 2017.

[27] J. Hult, "A fourth-order runge–kutta in the interaction picture method for simulating supercontinuum generation in optical fibers," *J. Lightw. Technol.*, vol. 25, no. 12, pp. 3770–3775, 2007.

[28] D. Deng, H. Zhang, Q. Gong, L. He, D. Li, and M. Gong, "Energy scalability of the dissipative soliton in an all-normal-dispersion fiber laser with nonlinear amplifying loop mirror," *Opt. Laser Technol.*, vol. 125, pp. 106010, 2020.

[29] G. Gao, *et al.*, "Chirp-coefficient bisection iteration method for phase-intensity reconstruction of chirped pulses," *Opt. Rev.*, vol. 25, no. 5, pp. 598–607, 2018.